Design, Analysis, and Integration of a New Two-Degree-of-Freedom Articulated Multi-Link Robotic Tail Mechanism

Yujiong Liu

Robotics and Mechatronics Lab, Department of Mechanical Engineering, Virginia Tech, Blacksburg, VA 24061 e-mail: yjliu@vt.edu

Pinhas Ben-Tzvi¹

Mem. ASME Robotics and Mechatronics Lab, Department of Mechanical Engineering, Virginia Tech, Blacksburg, VA 24061 e-mail: bentzvi@vt.edu

Based on observations from nature, tails are believed to help animals achieve highly agile motions. Traditional single-link robotic tails serve as a good simplification for both modeling and implementation purposes. However, this approach cannot explain the complicated tail behaviors exhibited in nature where multi-link structures are more commonly observed. Unlike its single-link counterpart, articulated multi-link tails essentially belong to the serial manipulator family which possesses special motion transmission design challenges. To address this challenge, a cable-driven hyper-redundant design becomes the most used approach. Limited by cable strength and elastic components, this approach suffers from low-frequency response, inadequate generated inertial loading, and fragile hardware, which are all critical drawbacks for robotic tails design. To solve these structure-related shortcomings, a multi-link robotic tail made up of rigid links is proposed in this paper. The new structure takes advantage of the traditional hybrid mechanism architecture, but utilizes rigid mechanisms to couple the motions between the ith link and the (i+1)th link rather than using cable actuation. By doing so, the overall tail becomes a rigid mechanism that achieves quasi-uniform spatial bending for each segment and allows performing highly dynamic motions. The mechanism and detailed design of this new robotic tail are presented. The kinematic model was developed and an optimization process was conducted to reduce the bending non-uniformity for the rigid tail. Based on this special optimization design, the dynamic model of the new mechanism is significantly simplified. A small-scale threesegment prototype was integrated to verify the proposed mechanism's unique mobility. [DOI: 10.1115/1.4045842]

Keywords: bio-inspired design, dynamics, mechanism design, mechanism synthesis, parallel platforms, robot design

1 Introduction

Tails are widely used in nature to help animals accomplish agile motions [1]. For instance, cheetah [2] is observed to use its tail to maneuver during hunting, monkeys [3] are observed to use tails to balance their motion on trees and grab branches as an additional arm, and kangaroos [4] are found to use tails to propel and power their locomotion. These fascinating animal tail behaviors attract both scientists and engineers to investigate further the tail functionalities and develop robotic tails [5].

As the first step, researchers abstracted the animal tail as a single-link pendulum. This approach brings about obvious benefits: by modeling and implementing the tail as a single rigid body, the analysis and prototyping can be simplified significantly. The research in Refs. [2,6–18] revealed that the tail has important effects on animal locomotion, especially for highly agile transient behaviors, such as accelerating, maneuvering, and stabilization. However, the single-link model has a fundamental drawback in that the animals in nature evolved multi-link tail structures [19]. This makes the single-link approach insufficient to explain the complicated tail behaviors exhibited in nature.

Therefore, multi-link tails are proposed for both modeling and implementation purposes. Theoretical research [20] shows that a multi-link tail design structure has the benefit of generating a higher inertial loading and volumetric center of the mass workspace.

Based on this finding, several multi-link robotic tails [21–26] were built to evaluate their practical performances. Hardware in the loop experiments and simulations [27,28] were also conducted to investigate the stabilization and maneuvering control of the tail on legged robot locomotion. However, due to the limitations of cable strength and elastic effects of the spring components, the tails were limited in responding to high-frequency input, which is critical for the successful implementation of highly dynamic robotic tails. The motivation of this work is to design new tail mechanisms that can address these design implementation-related shortcomings.

For multi-link tail designs, the current approaches roughly fit into two design paradigms based on their source of inspiration. The first paradigm evolved from work on continuum manipulators [29] by discretizing the continuum backbone into multiple links, where each link is driven by cables or rods. The tails belonging to this category (such as the tails in Refs. [23,24,26]) usually have a hyperredundant structure and thus require additional constraints. Similar to continuum robotic arms, elastic components are used to provide these constraints, as shown in Figs. 1(a) and 1(b). The other paradigm (such as the tails in Refs. [22,25]) is derived directly from engineering considerations. By analyzing the required mobility for maneuvering and stabilizing the mobile platform, it was found that two degrees-of-freedom (DOFs) planar bending combined with an additional overall rolling DOF might be adequate for these tasks.

However, both paradigms utilized cables to drive the system, which suffers from cable strength limitations and cable elasticity. Other common issues for cable-driven systems include unidirectional driving (requires more actuators and increases control complexity), unpredictable cable friction, and relatively

¹Corresponding author.

Contributed by the Mechanisms and Robotics Committee of ASME for publication in the JOURNAL OF MECHANISMS AND ROBOTICS. Manuscript received September 23, 2019; final manuscript received December 14, 2019; published online December 23, 2019. Assoc. Editor: Anurag Purwar.

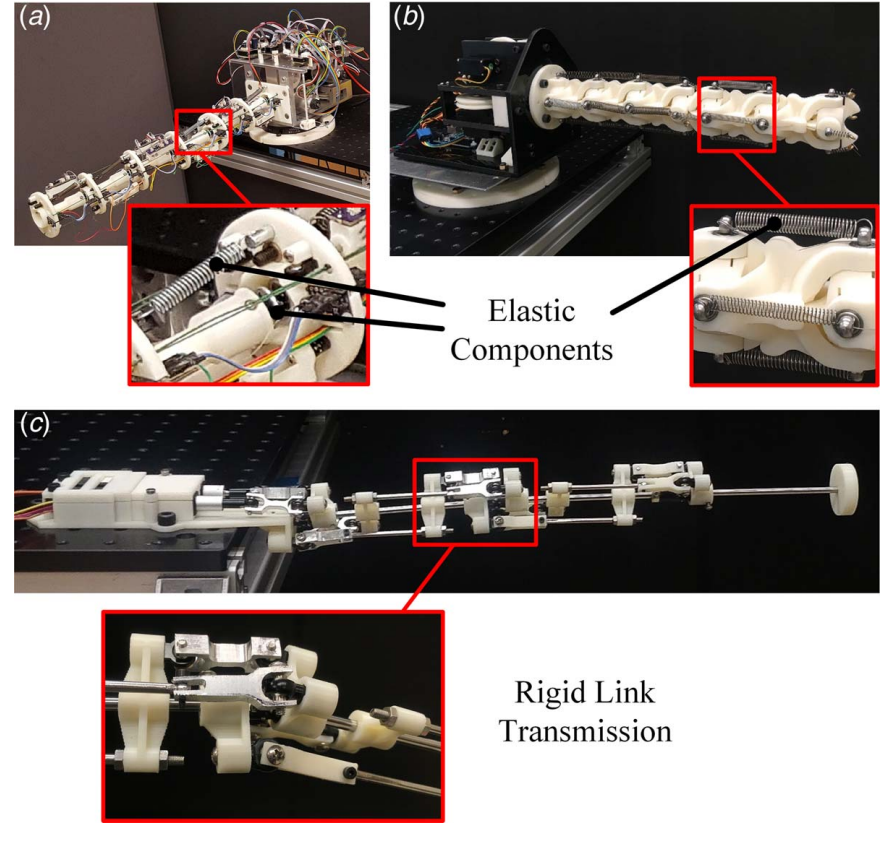


Fig. 1 Three examples of multi-link tails: (a) the USRT (Universal Spatial Robotic Tail) [24], (b) the RML (Robotics and Mechatronics Lab) tail [26], and (c) the Rigitail proposed in this paper. The USRT and the RML Tail both use elastic components (springs) to constrain the redundant DOFs while the Rigitail uses rigid links to constrain and transmit motion.

short lifetimes. These shortcomings worsen the low-frequency response problem introduced by the elastic components.

Therefore, this paper is motivated by looking for new multi-link tail mechanisms that are able to generate high momentums while having high stiffness. By analyzing the relationship between the mechanical structure and the performance, a new multi-link robotic tail (Fig. 1(c)) based on a novel rigid coupling hybrid mechanism (RCHM) concept is proposed. Corresponding kinematic analysis, dynamic modeling, and proof-of-concept prototyping are conducted to validate this new mechanism.

The rest of this paper is organized as follows. Section 2 analyzes the design requirements and introduces the rigid coupling hybrid mechanism concept. Section 3 substantiates the robotic tail design, presents the deductive process of realizing the required mechanism, and explains in detail the mechanical design. Section 4 develops the kinematic model for the proposed mechanism and Sec. 5 evaluates the theoretical performance based on the dynamical model. Finally, Sec. 6 presents the details of the prototype integration.

2 From Flexible Transmission Tail to Rigid Transmission Tail

As presented in the introduction, this paper is motivated by looking for rigid multi-link tails that can respond to high-frequency input and enable it to generate high momentum. This section analyzes the design requirements in further detail and addresses the challenge by introducing the rigid coupling hybrid mechanism.

Table 1 summarizes the mechanical structure of most existing robotic tails. Due to the simplicity and rigidity, a single-link structure is recognized as the most efficient and reliable way to inject momentum into the system. Compared with the popular single-link approach, relatively less research has been done for multi-link tails

although they generate higher momentum in theory, partially due to the complicated transmission design. For the current three multilink tails, Ref. [25] is recognized as a rigid tail due to its gear coupling mechanism and [24,26] are recognized as flexible tails due to their elastic backbone and springs. It turns out that the rigid one performs better in terms of dynamic performance than the flexible ones. However, since they all use cables to transmit motion from the base to each link, even the rigid one suffers from the common cable-driven issues such as unidirectional driving and cable elasticity. Therefore, if a multi-link structure that uses a rigid mechanism to transmit motion can be found, the new tail might be able to possess advantages seen in both single-link (high-frequency response, robust structure) and multi-link (high momentum, dexterous mobility) tails.

For this purpose, the difficulty lies in the motion transmission design, which requires transmitting motion for serially connected spatial mechanisms. To address this challenge, the RCHM is proposed. Here, the core idea is to transmit motion from the ith link to the (i+1)th link instead of transmitting directly from the base to each link. This transmission is realized by a "rigid coupling" mechanism that couples the motion of the (i+1)th link with that of the ith link. As for the basic mobility requirements, such as traditional hybrid mechanisms [30], the parallel mechanism part of the "hybrid mechanism" connects adjacent segments to achieve the required mobility. For instance, a 3-DOF spatial RCHM may be designed as a serially connected 3-DOF parallel mechanism with every adjacent parallel mechanism coupled by three rigid mechanisms.

As shown in Fig. 2, the complete RCHM consists of five components: base, actuation, link, parallel mechanism (PM), and rigid transmission mechanism (RTM). The RTMs realize the "rigid coupling" tasks for adjacent PMs, while the PMs realize the mobility tasks for the whole structure. Therefore, when the actuators drive

Table 1 Robotic tail structure review

Robots	Туре	DOF	Planar/spatial	Rigidity	Inter-link connection	Transmission
[6,7,9–13,15,16]	Single link	1	Planar	Rigid	_	Gear
[2,14]	Single link	2	Spatial	Rigid	_	Gear
[25]	Multi-link	3	Spatial	Rigid	Revolute Joint	Cable and Gear
[24,26]	Multi-link	>10	Spatial	Flexible	Universal Joint	Cable
[21,23]	Continuum	∞	Spatial	Flexible	Flexible Material	Cable

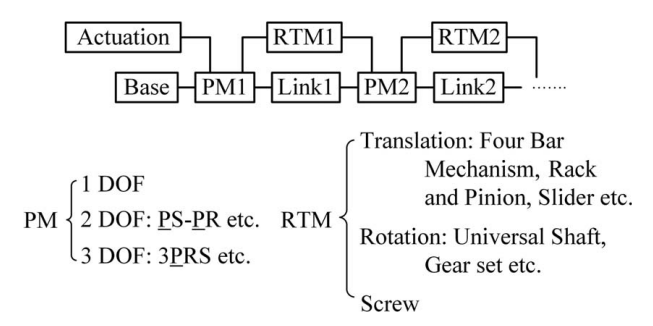


Fig. 2 The rigid coupling hybrid mechanism (RCHM) concept

PM1, the RTM1 will take advantage of the PM1 motion to drive PM2. As long as PM2 moves, RTM2 transmits motion from PM2 to PM3, and so on and so forth.

There are many PM designs [31] based on different mobility requirements, while there are only limited choices for the RTM designs. Figure 2 also lists several of the most useful designs including the four-bar mechanism, the rack and pinion mechanism, the slider mechanism (slider mechanism in this paper is used to describe a prismatic joint or a cylindrical joint that can transmit linear motion without change) for linear displacement transmission, and the universal shaft and gear set for rotary transmission. For different applications, the PMs and RTMs could be chosen to be the same or to be different.

3 System Design

Based on the proposed RCHM concept, this section presents the deductive process of realizing the conceptual robotic tail design. By analyzing the maneuvering and stabilization task requirements, the new tail is desired to have a rigid structure and achieve uniform spatial bending (more specifically, 2-DOF universal rotation), just like animal tails. Additionally, from an engineering perspective, since symmetry makes the manufacturing easier (parts are modular) and facilitates the kinematic and dynamic calculations (less kinematic variables), the new tail should be symmetric and reliable.

It is important to note that the PM could be subdivided into two halves: one "driving" half that drives the current segment's motion and another "measuring" half that measures the current segment's motion. The "measuring" half consists of passive chains, which does not affect the mobility of the "driving" half. Therefore, at

the first stage of the mechanism design, only the "driving" half is determined (the "driving" half totally determines the PM mobility). After determining the "driving" half, the "measuring" half can easily be added as passive chains while satisfying two conditions: (1) the passive chains do not affect the "driving" half and (2) the passive chains are able to measure the motion of the PM as desired. In practice, two identical, symmetrically placed (head-to-head) "driving" and "measuring" halves can usually satisfy both of the above requirements simultaneously. Since both the "driving" half and the "measuring" half consist of more than one chain, they are also referred to as PMs in this paper. In the following discussions, "U", "R", "P", "C" and "S" represent universal joint, revolute joint, prismatic joint, cylindrical joint and spherical joint, respectively. An underlined letter indicates an actuated joint.

3.1 Mechanism Design. Based on the RCHM concept and the above design process, the first step is to determine a parallel mechanism (mainly the "driving" PM) with 2-DOF rotation (specifically the universal rotation). This family of mechanisms is usually called 2R spherical mechanism or robotic wrist. A complete synthesis of this mechanism could be found in Refs. [32,33]. Depending on the number of kinematic chains, there are multiple candidates for this mechanism. For instance, if two chains are used to connect the *i*th link and the (i+1)th link, RR-RRR [34] and U-URR [35] might be good solutions (one example is shown in Fig. 3(a)). If three kinematic chains are used, 2RRR-RR [36] and 2PUS-U [37] might be good solutions (one example is shown in Fig. 3(b)). By applying the composite kinematic chains in Refs. [38,39], more solutions may be obtained. However, considering the desired mobility is exactly the universal rotation, a natural solution might be to use the universal joint directly as the basic kinematic chain and then use two other chains to drive the universal joint. This yields the choice of the 2PSS-U mechanism [40] as the "driving" PM, which has the benefits of decoupled universal rotations (with specific designs, one PSS chain could correspond to only one rotation of the universal joint) and hence simpler kinematics (because of the decoupled rotations). The three solutions are illustrated in Fig. 3.

The second step is to choose the appropriate rigid transmission mechanism to couple the motions between the ith link and the (i + 1)th link. For this purpose, Fig. 2 lists several candidates for different transmission tasks. In our case, due to the tail length, transmitting linear displacement is easier than transmitting rotation. Therefore, by narrowing the RTMs in Fig. 2, the four-bar mechanism, the rack and pinion mechanism, and the single slider mechanism become the most promising candidates. Figure 4 illustrates the motion transmitted by these mechanisms, where Figs. 4(b) and 4(d) follow the same motion direction and Figs. 4(a) and 4(c) reverse the

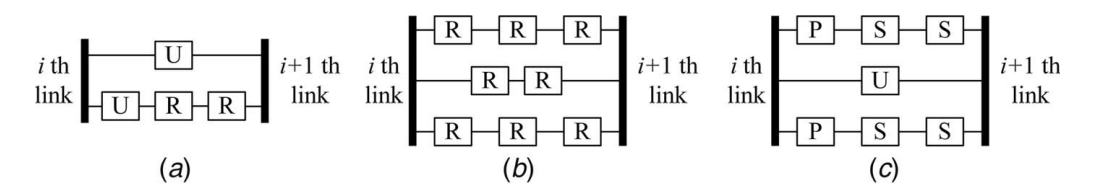


Fig. 3 Three examples of 2-DOF "driving" PM: (a) U-<u>U</u>RR configuration, (b) 2RRR-RR configuration, and (c) 2PSS-U configuration

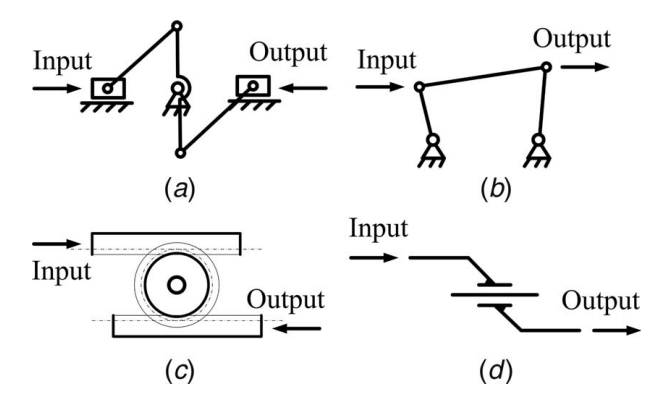


Fig. 4 Potential RTMs for linear displacement transmission: (a) slider-crank mechanism for motion reversing, (b) double rocker mechanism for motion following, (c) rack and pinion mechanism for motion reversing, and (d) single slider mechanism for motion following (the upper-half and the lower-half constitute the slider)

direction. Note that the 4R four-bar mechanism in Fig. 4(b) is not straightforward to be a promising candidate. However, considering its successful applications in planar cases [41], the 4R four-bar mechanism is still listed as a potential candidate here.

Different combinations of the PMs and RTMs generate different architectures of the final tail design. Considering both the mechanism simplicity and mechanical performance, the rigid tail mechanism is chosen as 2PSS-U being the "driving" PM and the slider mechanism being the RTM. For this "driving" PM, using the Grübler–Kutzbach criterion (G–K criterion) [42], the mobility is calculated as

$$M = 6n - \sum_{i=1}^{j} (6 - f_i) = 6 \times 5 - 4 - 2 \times (5 + 3 + 3) = 4$$
 (1)

where n is the number of moving bodies, j is the number of joints, and f_i is the corresponding joint's DOFs. Since SS chain has an internal DOF (the rotation with respect to the axis that goes through the two centers of the ball joints) which does not affect the overall mobility, the final mobility for 2PSS-U is 4-2=2.

3.2 Mechanical Design. Based on the mechanism in Sec. 3.1, this section realizes the mechanical design by mainly considering

the kinematic calculations and manufacturing cost. This means that the preferred design should make the kinematic calculation as simple as possible. For this purpose, modular/symmetric parts are preferred so that the number of dimensional variables is kept to a minimum. The preferred design should also make manufacturing as easy/low-cost as possible. For this purpose, the R joint is generally preferred over S joint due to its easier manufacturability. Similarly, the C joint is preferred over the P joint since the C joint does not need the design of a slot/key on the central rod to constrain the rotational motion.

The overall design of the new tail is shown in Fig. 5. This new tail design will be referred to as Rigitail for presentation convenience henceforth. The Rigitail consists of seven segments connected serially by universal joints. The universal joint is driven by two perpendicular PSS chains, which are denoted by chain A and chain B, respectively. Chain A and chain B along with the universal joint constitute the "driving" parallel mechanism (PM). To take advantage of the current segment motion for driving the next segment, an identical but head-to-head placed PM (sharing the same universal joint) is designed as the rigid coupling mechanism. This symmetric design results in a unique kinematic advantage that the input displacements for the (i+1)th segment can be obtained by computing the inverse kinematics of the PM for interchanged rotation angles (see Sec. 4.2). Chain A and chain B are also designed to be identical so that the yaw and pitch rotations have the same property.

Another important design feature lies in the placement of the ball joint. As shown in Fig. 5, $\mathbf{s}_{i,a3}$ has the same direction as \mathbf{z}_i . This makes chain A become a planar mechanism with kinematics that is independent of chain B. However, chain B is still a spatial mechanism affected by chain A. This feature facilitates the kinematic computation of the PM and more importantly, allows changing the first ball joint to a revolute joint. By doing so, the slider no longer needs to be constrained by the shaft (thus, the P joints are relieved as C joints) and the manufacturing complexity is reduced accordingly. It is worth to note that for the "measuring" PM, due to the symmetric design, chain B becomes the planar mechanism while chain A is the affected one. Figure 6 illustrates the kinematic diagram of the adjacent segment connection mechanism.

For this modified "driving" PM <u>CRS-CSS-U</u>, the mobility is calculated as

$$M = 6 \times 5 - 4 - 4 - 5 - 3 - 4 - 3 - 3 = 4$$
 (2)

Excluding one SS chain internal DOF, there are 3-DOFs left: (1) the translation of the first C joint, (2) the translation of the second C joint, and (3) the rotation of the second C joint. However, due to the

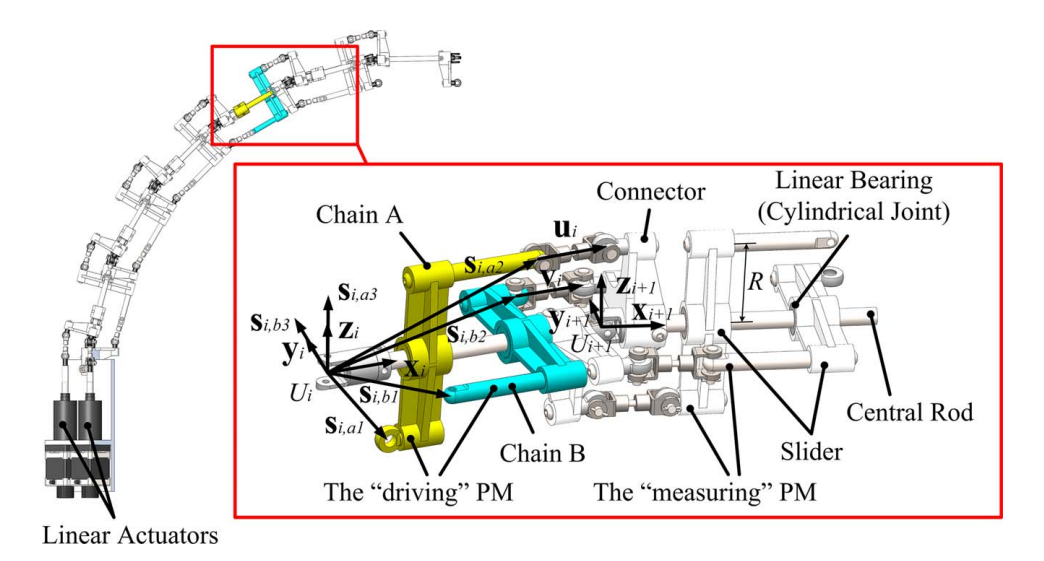


Fig. 5 Mechanical design of the Rigitail. Two identical PMs are placed head-to-head to connect adjacent links, which facilitates the kinematic calculation significantly.

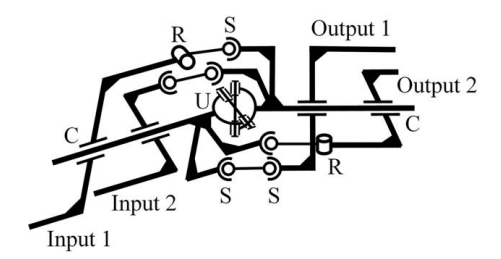


Fig. 6 Kinematic diagram of the segment connection mechanism

constraint of chain B from the previous segment, the third DOF is actually infeasible (referring to the far-right C joint in Fig. 6, its rotational DOF is restricted by the R joint). Therefore, the modified "driving" PM still has 2-DOFs. Note that the constraints for the first segment are guaranteed by the linear actuator, which is the P joints.

For the final PM in Fig. 6, the mobility is calculated as

$$M = 6 \times 9 - 4 - 2 \times (4 + 5 + 3) - 2 \times (4 + 3 + 3) = 6$$
 (3)

Excluding two internal DOFs, there are four left, out of which two rotational DOFs of the C joints are actually infeasible (constrained by adjacent segments). Therefore, the five-chain final PM has 2-DOFs.

4 Kinematic Analysis

This section presents the kinematic model of the Rigitail. Due to the hybrid mechanism architecture and the uniform design of each segment, the kinematics is obtained recursively.

4.1 Closed Form Segment-Wise Kinematics. In robotics, the kinematics problem usually consists of two sub-problems: (a) the forward kinematics that calculates the robot position and orientation given the actuator positions and (b) the inverse kinematics that calculates the actuator positions based on the given robot pose. For hybrid mechanisms [30], due to the overall serial structure and the segment-wise parallel structure, the kinematics has two levels: the overall level kinematics that determines the overall kinematics of the hybrid structure and the segment-level kinematics that determines the segment-wise kinematics. For the segment-level kinematics, the forward and inverse kinematics are no more than the traditional parallel mechanism kinematics. For the overall level kinematics, depending on specific cases, the kinematics calculation may need to be conducted from the root segment to the tip segment (forward propagation) or from the tip segment to the root segment (backward propagation), or by solving all segments simultaneously. The same procedure is applied to Rigitail. The segment-wise kinematics is derived first and the overall kinematics is then derived based on the segment-wise kinematics. The only difference is that due to the symmetric design, when computing the overall kinematics, the Rigitail does not discriminate the forward or backward propagation (i.e., calculating from the root to the tip and calculating from the tip to the root result in the same segment-wise kinematics).

Due to the symmetric design of chain A and chain B, the connection between adjacent segments essentially consists of two identical PMs (the "driving" PM and the "measuring" PM) that are placed head-to-head (specifically, in a central symmetric way with respect to the center of the universal joint). Therefore, the segmentwise kinematic calculation needs both the forward and inverse kinematics of the "driving" PM and the "measuring" PM. Mathematically, this requires two basic maps and their inverses: (a) the map $\alpha(a_i)$ from a_i to rotation α_{i+1} (α_{i+1} only depends on a_i due to the decoupled design), and (b) the map $\beta(\alpha_i, b_i)$ from a_i and b_i to β_{i+1} , where α_{i+1} , β_{i+1} , a_i , and b_i are implicitly defined in Eqs. (4) and (5).

Based on the kinematic configuration defined in Fig. 5, the homogenous transformation of the body fixed frame $\sum U_{i+1} = (U_{i+1}, \mathbf{x}_{i+1}, \mathbf{y}_{i+1}, \mathbf{z}_{i+1})$ on link i+1 with respect to $\sum U_i$ is

$${}^{i}\mathbf{T}_{i+1} = \mathbf{D}_{x}(L)\mathbf{R}_{y}(\alpha_{i+1})\mathbf{R}_{z}(\beta_{i+1})$$

$$\tag{4}$$

where \mathbf{R}_z and \mathbf{R}_y are the elementary rotational homogenous transformations for the *z*-axis and the *y*-axis, respectively. $\mathbf{D}_x(L)$ is the pure translation homogenous transformation along the *x*-axis for *L* (link length). The necessary local vectors are given in Eq. (5) where *R* is the tail radius (half of the width of the slider bar, as seen in Fig. 5), a_i and b_i are the displacement variables for the prismatic joints A and B, respectively.

$$i\mathbf{s}_{i,a2} = \begin{bmatrix} a_i & 0 & R & 1 \end{bmatrix}^{\mathrm{T}}$$

$$i\mathbf{s}_{i,a3} = \begin{bmatrix} 0 & 0 & R & 1 \end{bmatrix}^{\mathrm{T}}$$

$$i\mathbf{s}_{i,b2} = \begin{bmatrix} b_i & R & 0 & 1 \end{bmatrix}^{\mathrm{T}}$$

$$i\mathbf{s}_{i,b3} = \begin{bmatrix} 0 & R & 0 & 1 \end{bmatrix}^{\mathrm{T}}$$

$$(5)$$

Therefore, the constraint equations are obtained as

$$\mathbf{u}_i^T \mathbf{u}_i = \mathbf{v}_i^T \mathbf{v}_i = e^2 + 1 \tag{6}$$

where e is the bar length between the two ball joints and

$${}^{i}\mathbf{u}_{i} = {}^{i}\mathbf{T}_{i+1}{}^{i+1}\mathbf{s}_{i+1,a3} - {}^{i}\mathbf{s}_{i,a2}$$
 (7)

$${}^{i}\mathbf{v}_{i} = {}^{i}\mathbf{T}_{i+1}{}^{i+1}\mathbf{s}_{i+1,b3} - {}^{i}\mathbf{s}_{i,b2}$$
 (8)

Solving Eq. (6) yields α and β

$$\alpha_{i+1} = \alpha(a_i) = \cos \frac{2R^2 + (L - a_i)^2 - e^2}{2R\sqrt{R^2 + (L - a_i)^2}} - \tan \frac{L - a_i}{R}$$
 (9)

$$\beta_{i+1} = \beta(\alpha_i, b_i) = -a\cos\frac{2R^2 + (L - b_i)^2 - e^2}{2R\sqrt{R^2 + (L - b_i)^2 c_\alpha^2}} + a\tan\frac{(L - b_i)c_\alpha}{R}$$

where $s_{\alpha} = \sin \alpha_{i+1}$, $c_{\alpha} = \cos \alpha_{i+1}$, and $C = 2R^2 + (L - b_i)^2 - e^2$. The inverses of α and β are obtained by solving Eq. (6) for a_i and b_i

$$a_i = \alpha^{-1}(\alpha_{i+1}) = L + Rs_\alpha - \sqrt{e^2 - R^2(1 - c_\alpha)^2}$$
 (11)

$$b_{i} = \beta^{-1}(\alpha_{i+1}, \beta_{i+1}) = L - Rc_{\alpha}s_{\beta} - \sqrt{e^{2} - R^{2}(1 - c_{\beta})^{2} - R^{2}s_{\alpha}^{2}s_{\beta}^{2}}$$
(12)

where $s_{\beta} = \sin \beta_{i+1}$ and $c_{\beta} = \cos \beta_{i+1}$.

4.2 Overall Kinematics Propagation. The overall kinematics is obtained by propagating the segment-wise kinematics. Again, due to the head-to-head identical PM feature for each segment, the overall kinematics has the same form for both the forward kinematics and the inverse kinematics. Therefore, based on the forward maps α , β , and their inverses, the (i+1)th segment displacement $\mathbf{d}_{i+1} = \begin{bmatrix} a_{i+1} & b_{i+1} \end{bmatrix}^{\mathrm{T}}$ may be calculated from the ith segment displacement \mathbf{d}_i

$$\mathbf{d}_{i+1} = \mathbf{d}(\mathbf{d}_i) = \begin{bmatrix} 2L - 2e - \beta^{-1}(\beta(\alpha_i, b_i), \alpha(a_i)) \\ 2L - 2e - \alpha^{-1}(\beta(\alpha_i, b_i)) \end{bmatrix}$$
(13)

where d is the vector function mapping the adjacent segment displacements. Then, the kinematics from the ith segment to the jth segment (assuming j > i without loss of generality) is calculated as

$$\mathbf{d}_i = d^{j-i}(\mathbf{d}_i) \tag{14}$$

where (j-i)th power refers to the function composition. The global position and orientation of each link is computed as

$${}^{0}\mathbf{T}_{i} = \prod_{k=1}^{i} {}^{k-1}\mathbf{T}_{k} \tag{15}$$

4.3 Workspace Analysis. The workspace is defined as the points that the tail tip can reach in 3D space. Due to the 2-DOFs, the Rigitail's workspace is a surface area. Using the design parameters L=62 mm, R=19 mm, and e=19 mm, half of the workspace (the upper-half is symmetric to the bottom-half) is plotted in Fig. 7, where the starred line illustrates one sample configuration.

Using the center of mass (COM) angle as the yardstick, a multi-link tail usually has a larger workspace than a single-link pendulum due to its curvature (as shown in Refs. [24,25]). Due to the small rotation range (limited to $\pm 20\deg$) of each PM, the workspace is free of singularities. This makes the Rigitail a robust and simple solution for multi-link tails.

4.4 Reducing the Bending Non-uniformity. For multi-link tails, achieving uniform bending facilitates the kinematic and dynamic computations significantly. That is, if one segment rotations are known, the rotations for the rest of the segments are known immediately without computation. However, Eq. (13) shows that d is a nonlinear mapping depending on the design parameters. Therefore, an optimization process is necessary to reduce the nonlinearity as much as possible.

Since α and β are both smooth bijections in the workspace, the uniform bending can be measured by the difference between \mathbf{d}_{i+1} and \mathbf{d}_i , which basically means that if the following segment displacement input \mathbf{d}_{i+1} always mimics the current segment input displacement \mathbf{d}_i , then the displacement input for all segments is the same, and thus, all segments produce the same bending. Therefore, the bending non-uniformity is defined by

$$\delta \mathbf{d} = \mathbf{d}_{i+1} - \mathbf{d}_i \tag{16}$$

and the following section reduces the $\delta \mathbf{d}$ term.

To minimize the bending non-uniformity, Eq. (16) is evaluated first by substituting α^{-1} and β^{-1} in Eqs. (11) and (12), which yields

$$\frac{\delta \mathbf{d}}{R} = \begin{bmatrix} c_{\beta} s_{\alpha} - s_{\alpha} + F_{\lambda} (1 - c_{\alpha}) \\ c_{\alpha} s_{\beta} - s_{\beta} + F_{\lambda} (1 - c_{\beta}) \end{bmatrix}$$
(17)

where $\lambda = e/R$ is a dimensionless coefficient for optimization and $F_{\lambda}(x)$ is the function generating the detailed expressions of Eq. (17). Note that the non-uniformity does not depend on L.

$$F_{\lambda}(x) = \sqrt{\lambda^2 - x^2 - s_{\beta}^2 s_{\alpha}^2} + \sqrt{\lambda^2 - x^2} - 2\lambda \tag{18}$$

Equation (17) expresses the non-uniformity distribution for different bending angles α_{i+1} and β_{i+1} . For optimization purposes, the bending region is chosen as $\mathcal{D} = [-\pi/12\pi/12] \times [-\pi/12\pi/12]$, which is reasonable for a seven-link tail. Therefore,

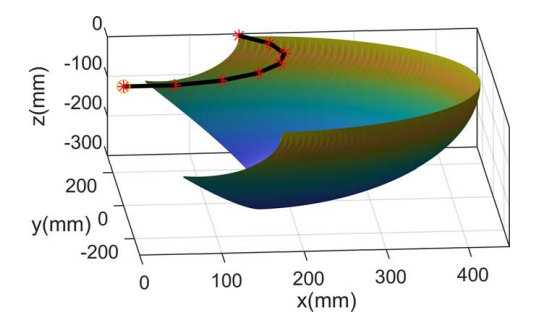


Fig. 7 Bottom half of the Rigitail workspace

the scalar k

$$k(\lambda) = \int_{\mathcal{D}} \| \delta \mathbf{d} \| / \mathbf{R}$$
 (19)

may be defined to reflect the overall non-uniformity.

Simple computation (shown in Fig. 8) shows that k is monotonically decreasing as λ is increasing. However, k is decreasing slowly after $\lambda > 1$. From practical considerations, large λ shrinks the space for mounting two sliders. Therefore, the optimized λ is chosen to be 1 as a trade-off. Figure 9 shows the non-uniformity distribution in region \mathcal{D} for $\lambda = 1$ and $\lambda = 0.3$. The maximum value of 0.0173 appears at the region vertices (which is equivalent to max ($\|\delta \mathbf{d}\|$) = 0.33 mm for the practical design).

5 Dynamic Model

Due to the special design described in Sec. 4.4 to reduce the bending non-uniformity, each universal joint achieves almost the same rotation inside its workspace ($\pm 20^{\circ}$). This brings in a significant advantage for dynamic analysis that if one segment's kinematics is known, and the kinematic information for the rest of the segments can be obtained without computation. Therefore, the following assumption is made.

A1: Every universal joint achieves the same rotation.

In addition, since the relative motion of the sliders with respect to its central rod is small in comparison with its absolute motion in the global frame, an additional assumption is made to simplify the dynamics.

A2: The relative motion of the sliders with respect to its center rod is negligible.

This assumption allows modeling the whole assembly between two adjacent universal joints as one solid body and implicitly neglects the friction between the sliders and the central rod. This solid body is also called link i in the dynamic modeling.

Additional assumptions for dynamic modeling include ideal joints without friction and rigid links without elasticity. Note that

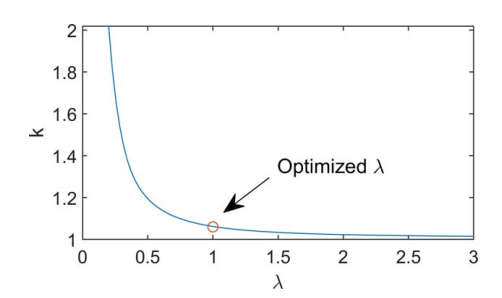


Fig. 8 k is monotonic decreasing as λ increases

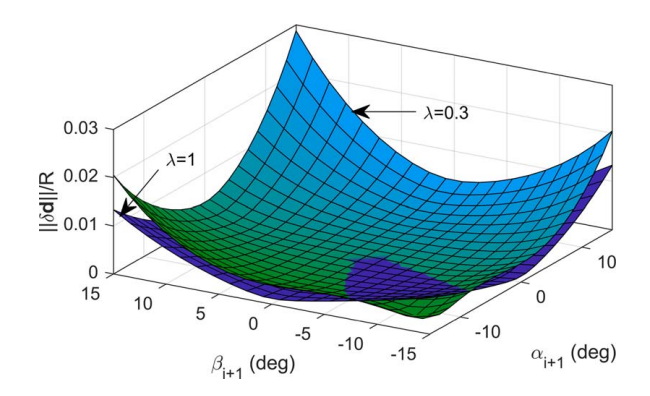


Fig. 9 The $\|\delta d\|/R$ distribution for optimized $\lambda=$ 1 and non-optimized $\lambda=$ 0.3

under these assumptions, Rigitail model is able to respond to any high-frequency input (using non-bounded actuators).

5.1 Equation of Motion. Based on assumptions A1 and A2, the dynamic model of the Rigitail is simplified as a traditional serial manipulator model except that all its joints execute the same motion. As shown in Fig. 10, $\sum S = (U_1, \mathbf{x_0}, \mathbf{y_0}, \mathbf{z_0})$ is the inertial frame and it coincides with $\sum U_1$ when the universal joint rotations are all zero. The generalized coordinates are selected as $\mathbf{q} = \begin{bmatrix} \alpha_1 & \beta_1 \end{bmatrix}^T$. Therefore, based on the principle of virtual work, the equation of motion is obtained as

$$\mathbf{J}_{a}^{T}\mathbf{f} = \sum_{i=1}^{6} \mathbf{J}_{i,c}^{T} m(\dot{\mathbf{v}}_{i,c} - [0, 0, -g]^{T}) + \mathbf{J}_{i,\omega}^{T} (\mathbf{I}_{i} \dot{\boldsymbol{\omega}}_{i} + \tilde{\boldsymbol{\omega}}_{i} \mathbf{I}_{i} \boldsymbol{\omega}_{i})$$
(20)

where m is the link mass and \mathbf{f} is the actuation force. $\mathbf{v}_{i,c}$ is the linear velocity of the ith link COM and $\boldsymbol{\omega}_i$ is its angular velocity. \mathbf{J}_a , $\mathbf{J}_{i,c}$, and $\mathbf{J}_{i,\omega}$ are the Jacobians that map actuation force, linear inertial loading, and rotational inertial loading on the generalized space, respectively. \mathbf{I}_i is the moment of inertia of the ith link with respect to its COM, and \mathbf{I}_i is computed by Eq. (21) in which \mathbf{R}_i is the link orientation (extracted from \mathbf{T}_i) and i \mathbf{I}_i is the body fixed inertia matrix (constant matrix).

$$\mathbf{I}_i = \mathbf{R}_i^{\ i} \mathbf{I}_i \mathbf{R}_i^T \tag{21}$$

To find the acceleration information in Eq. (20), position relationships need to be derived first. By using recursive kinematics, the COM position $\mathbf{p}_{i,c}$ of the *i*th link is obtained as

$$\mathbf{p}_{i,u2u} = L\mathbf{x}_i \tag{22}$$

$$\mathbf{p}_{i\,u2c} = \mathbf{p}_{i\,u2u}/2\tag{23}$$

$$\mathbf{p}_{i,u} = \mathbf{p}_{i-1,u} + \mathbf{p}_{i-1,u2u}$$
 (24)

$$\mathbf{p}_{i,c} = \mathbf{p}_{i,u} + \mathbf{p}_{i,u2c} \tag{25}$$

where the COM is assumed to be located at the geometric center of the link and the initial condition is $\mathbf{p}_{1,u} = \mathbf{0}_{3\times 1}$. Differentiating the position relationships yields the velocity propagation equations

$$\mathbf{v}_{i,u} = \mathbf{v}_{i-1,u} + \mathbf{\omega}_{i-1} \times \mathbf{p}_{i-1,u2u}$$
 (26)

$$\mathbf{v}_{i,c} = \mathbf{v}_{i,u} + \mathbf{\omega}_i \times \mathbf{p}_{i,u2c} \tag{27}$$

$$\mathbf{\omega}_i = i\mathbf{\omega}_1 = i(\dot{\alpha}_1 \mathbf{y}_0 + \dot{\beta}_1 \mathbf{z}_1) \tag{28}$$

where the initial condition is $\mathbf{v}_{1,u} = \mathbf{0}_{3\times 1}$. Based on the velocity relationships, the recursive Jacobians could be obtained as well

$$\mathbf{J}_{i,u} = \mathbf{J}_{i-1,u} - \tilde{\mathbf{p}}_{i-1,u2u} \mathbf{J}_{i-1,\omega}$$
 (29)

$$\mathbf{J}_{i,c} = \mathbf{J}_{i,u} - \tilde{\mathbf{p}}_{i,u2c} \mathbf{J}_{i,\omega} \tag{30}$$

$$\mathbf{J}_{i,\omega} = i\mathbf{J}_{1,\omega} = i\begin{bmatrix} \mathbf{y}_0 & \mathbf{z}_1 \end{bmatrix} \tag{31}$$

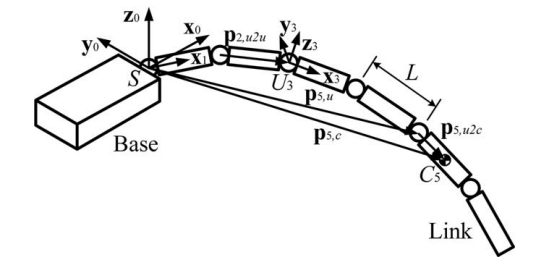


Fig. 10 Dynamic model of the Rigitail

in which the initial condition is $\mathbf{J}_{1,u} = \mathbf{0}_{3\times 2}$. Similarly, the accelerations are obtained by differentiating the velocities

$$\dot{\mathbf{v}}_{i,u} = \dot{\mathbf{v}}_{i-1,u} + \widetilde{\dot{\mathbf{o}}}_{i-1} \mathbf{p}_{i-1,u2u} + \widetilde{\mathbf{o}}_{i-1}^2 \mathbf{p}_{i-1,u2u}$$
(32)

$$\dot{\mathbf{v}}_{i,c} = \dot{\mathbf{v}}_{i,u} + \widetilde{\boldsymbol{\omega}}_{i} \mathbf{p}_{i,u2c} + \widetilde{\boldsymbol{\omega}}_{i}^{2} \mathbf{p}_{i,u2c}$$
 (33)

$$\dot{\mathbf{\omega}}_i = i\dot{\mathbf{\omega}}_1 = i(\ddot{\alpha}_1 \mathbf{y}_0 + \ddot{\beta}_1 \mathbf{z}_1 + \dot{\beta}_1 \tilde{\mathbf{\omega}}_1 \mathbf{z}_1) \tag{34}$$

The only term requiring special treatment is the J_a , which needs a further analysis on the segment-wise kinematics of the first joint. Differentiating Eqs. (11) and (12) for the first joint yields

$$\dot{a}_0 = \left(Rc_\alpha + \frac{s_\alpha - s_\alpha c_\alpha}{\sqrt{\lambda^2 - (1 - c_\alpha)^2}} \right) \dot{\alpha}_1 \tag{35}$$

$$\dot{b}_0 = Rs_{\alpha}s_{\beta}\dot{\alpha}_1 - Rc_{\alpha}c_{\beta}\dot{\beta}_1 + \frac{s_{2\alpha}s_{\beta}^2\dot{\alpha}_1 + (2s_{\beta} - s_{2\beta} + s_{\alpha}^2s_{2\beta})\dot{\beta}_1}{2\sqrt{\lambda^2 - (1 - c_{\beta})^2 - s_{\alpha}^2s_{\beta}^2}}$$
(36)

Therefore, $J_a \in \mathbb{R}^{2\times 2}$ could be obtained by writing Eqs. (35) and (36) into a matrix form such that

$$\begin{bmatrix} \dot{a}_0 \\ \dot{b}_0 \end{bmatrix} = \mathbf{J}_a \begin{bmatrix} \dot{\alpha}_1 \\ \dot{\beta}_1 \end{bmatrix} \tag{37}$$

5.2 Momentum Potentials. Since the Rigitail design is motivated by achieving maneuvering and stabilization tasks for legged robots, the dynamic performance is mainly measured by the momentum that the tail injects into the system. This section calculates the momentum potentials that the Rigitail may achieve compared with the traditional single-link pendulum tail. For this computation, all links are further simplified as evenly distributed cylinders.

The moment of momentum [43] of the Rigitail is calculated by Eq. (38) where the subscript "rt" stands for "rigid tail" ("pt" stands for "pendulum tail" in the following equations).

$$\mathbf{h}_{rt} = \sum_{i=1}^{6} \left(\mathbf{I}_{i} \mathbf{\omega}_{i} + m \mathbf{p}_{i,c} \times \mathbf{v}_{i,c} \right)$$
 (38)

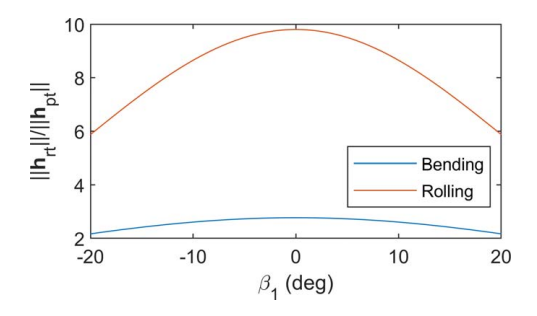


Fig. 11 The momentum comparison between the Rigitail and the pendulum tail

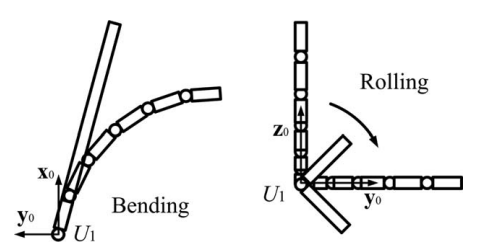


Fig. 12 Two typical tail motions show that a multi-link structure generates more momentum than a single-link structure with the same input

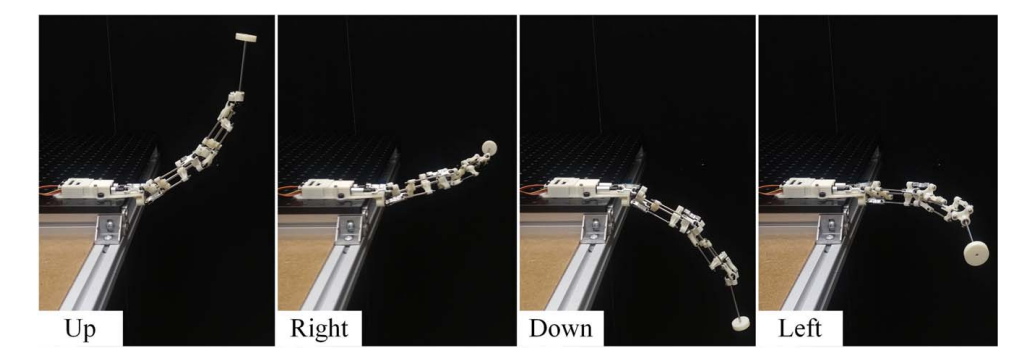


Fig. 13 A three-segment proof-of-concept prototype integration of the Rigitail

Based on the cylinder assumption, ${}^{i}\mathbf{I}_{i}$ is obtained as

$${}^{i}\mathbf{I}_{i} = \operatorname{Diag}(\begin{bmatrix} 0 & mL^{2}/12 & mL^{2}/12 \end{bmatrix}) \tag{39}$$

For a same length, same weight single-link pendulum tail, the moment of momentum is calculated as

$$\mathbf{h}_{pt} = \mathbf{I}_{pt}\mathbf{\omega}_1 + 6m\mathbf{p}_{pt,c} \times (\mathbf{\omega}_1 \times \mathbf{p}_{pt,c})$$
 (40)

where ω_1 indicates the same rotation as the first link of the Rigitail. The moment of inertia I_{pt} and $p_{pt,c}$ are given by

$$\mathbf{I}_{pt} = \mathbf{R}_1 \operatorname{Diag}(\begin{bmatrix} 0 & 18mL^2 & 18mL^2 \end{bmatrix}) \mathbf{R}_1^T$$
 (41)

$$\mathbf{p}_{pt,c} = \mathbf{R}_1 \begin{bmatrix} 3L & 0 & 0 \end{bmatrix}^{\mathrm{T}} \tag{42}$$

To compare the momentum generated by the Rigitail and a pendulum tail, numerical computations of two typical cases were conducted: planar bending and rolling. As shown in Fig. 11, the value $\|\mathbf{h}_{rt}\| / \|\mathbf{h}_{pt}\|$ is used to compare the momentum and different orientations β_1 were tested. It can be found that the Rigitail generates much larger momentum than the pendulum tail and both ratios maximize at $\beta_1 = 0$. It is worth to note that the rolling ratio is not defined at $\beta_1 = 0$ since both \mathbf{h}_{pt} and \mathbf{h}_{rt} are zero vectors at this point.

The advantages can be explained intuitively. As shown in Fig. 12, for the same rotation input, the Rigitail has a similar moment of inertia as the pendulum tail when bending. However, each segment in the Rigitail possesses much larger velocity than the corresponding segment in the pendulum if the pendulum is regarded as a fixed connected multi-link structure. As for rolling, although both structures have the same angular velocity, the Rigitail possesses much larger moment of inertia.

6 Prototype Validation

To validate the feasibility of the proposed new mechanism, a small scale (L=111 mm, R=16 mm) three-segment proof-of-concept prototype was built, as shown in Fig. 13. To prevent elastic bending, 4 mm stainless steel rods were used as the central rod. The sliders and the connectors on each rod end were made by 3D printing with ABS plastic. To enhance the structure's strength, all the ball joints (aluminum), connecting linkages (steel and aluminum), and lock pins (steel) for the first two segments were made out of metal. Two Firgelli linear actuators (L12-30-210-6P) were used to drive the robotic tail. Due to the small size, linear bearings for the sliders were not incorporated. Since each segment is designed to have identical features, the prototype could be elongated easily by adding additional identical segments.

Figure 13 shows four configurations of the Rigitail which verifies the mobility of the proposed mechanism. However, limited by the speed of the linear actuators, the proposed highly dynamic motions (e.g., high-frequency response tests) are not yet demonstrable.

7 Conclusion

By taking advantage of the traditional hybrid mechanism architecture and utilizing rigid mechanisms to couple the motions between the *i*th link and the (i+1)th link, this paper proposed a new spatial multi-link robotic rigid tail mechanism. The new tail realizes the rigid coupling hybrid mechanism concept with 2PSS-U being the parallel mechanism and the slider mechanism being the rigid transmission mechanism. By arranging the tail mechanism in such a manner, the new tail is able to achieve 2-DOF universal bending for each segment and is driven by only two linear actuators. Due to the rigid structure, the tail has promising potential in high-stiffness, high-speed application scenarios. The kinematic model was developed, and an optimization process was conducted to reduce the bending non-uniformity. Because of this specially optimized design, a significantly simplified dynamic model was obtained. A theoretical momentum performance evaluation further showed the dynamic potential of the proposed new mechanism. To demonstrate this unique mechanism, a small-scale, three-segment proof-of-concept prototype was manufactured and integrated.

Future work will mainly focus on implementing a full-scale tail prototype to evaluate its proposed highly dynamic performances. After building the prototype, comparison tests with its flexible counterparts (cable-driven robotic tails) will be conducted to evaluate its high-frequency response capability. In addition, detailed dynamic modeling including joint friction and actuator saturation effects may also be required. The validated prototype will then be mounted on a legged robot to further investigate its practical performances for maneuvering and stabilization tasks.

Acknowledgment

The authors would like to thank Shikhar Kashyap for his assistance in prototyping the Rigitail.

Funding Data

 This material is based upon work supported by the National Science Foundation under Grant No. 1906727; Funder ID: 10.13039/501100008982.

References

- [1] Hickman, G. C., 1979, "The Mammalian Tail: A Review of Functions," Mammal Rev., 9(4), pp. 143–157.
- [2] Patel, A., and Boje, E., 2015, "On the Conical Motion of a Two-Degree-of-Freedom Tail Inspired by the Cheetah," IEEE Trans. Rob., 31(6), pp. 1555–1560.
- [3] Young, J. W., Russo, G. A., Fellmann, C. D., Thatikunta, M. A., and Chadwell, B. A., 2015, "Tail Function During Arboreal Quadrupedalism in Squirrel Monkeys (Saimiri Boliviensis) and Tamarins (Saguinus Oedipus)," J. Exp. Zool. A Ecol. Genet. Physiol., 323(8), pp. 556–566.
- [4] O'Connor, S. M., Dawson, T. J., Kram, R., and Donelan, J. M., 2014, "The Kangaroo's Tail Propels and Powers Pentapedal Locomotion," Biol. Lett., 10(7), p. 20140381.

- [5] Saab, W., Rone, W. S., and Ben-Tzvi, P., 2018, "Robotic Tails: A State-of-the-Art Review," Robotica, 36(9), pp. 1263–1277.
- [6] Liu, G. H., Lin, H. Y., Lin, H. Y., Chen, S. T., and Lin, P. C., 2014, "A Bio-Inspired Hopping Kangaroo Robot With an Active Tail," J. Bionic Eng., 11(4), pp. 541–555.
- [7] De, A., and Koditschek, D. E., 2015, "Parallel Composition of Templates for Tail-Energized Planar Hopping," IEEE International Conference on Robotics and Automation, Seattle, May 26–30, pp. 4562–4569.
- [8] Liu, Y., and Ben-Tzvi, P., 2018, "Dynamic Modeling of a Quadruped With a Robotic Tail Using Virtual Work Principle," Proceedings of the IDETC/CIE, Quebec City, Canada, Aug. 26–29, p. V05BT07A021.
- [9] Libby, T., Moore, T. Y., Chang-Siu, E., Li, D., Cohen, D. J., Jusufi, A., and Full, R. J., 2012, "Tail-Assisted Pitch Control in Lizards, Robots and Dinosaurs," Nature, 481(7380), pp. 181–184.
- [10] Briggs, R., Lee, J., Haberland, M., and Kim, S., 2012, "Tails in Biomimetic Design: Analysis, Simulation, and Experiment," IEEE/RSJ International Conference on Intelligent Robots and Systems, Vilamoura, Portugal, Oct. 7–12, pp. 1473–1480.
- [11] Zeglin, G. J., 1991, "Uniroo—A One Legged Dynamic Hopping Robot," Bachelor thesis, Massachusetts Institute of Technology, Boston, MA.
- [12] Jusufi, A., Kawano, D. T., Libby, T., and Full, R. J., 2010, "Righting and Turning in Mid-Air Using Appendage Inertia: Reptile Tails, Analytical Models and Bio-Inspired Robots," Bioinspiration Biomimetics, 5(4), p. 045001.
- [13] Chang-Siu, E., Libby, T., Tomizuka, M., and Full, R. J., 2011, "A Lizard-Inspired Active Tail Enables Rapid Maneuvers and Dynamic Stabilization in a Terrestrial Robot," IEEE/RSJ International Conference on Intelligent Robots and Systems, San Francisco, CA, Sept. 25–30, pp. 1887–1894.
- [14] Chang-Siu, E., Libby, T., Brown, M., Full, R. J., and Tomizuka, M., 2013, "A Nonlinear Feedback Controller for Aerial Self-Righting by a Tailed Robot," IEEE International Conference on Robotics and Automation, Karlsruhe, Germany, May 6–10, pp. 32–39.
- [15] Heim, S. W., Ajallooeian, M., Eckert, P., Vespignani, M., and Ijspeert, A. J., 2016, "On Designing an Active Tail for Legged Robots: Simplifying Control Via Decoupling of Control Objectives," Ind. Robot., 43(3), pp. 338–346.
- [16] Casarez, C. S., and Fearing, R. S., 2018, "Steering of an Underactuated Legged Robot Through Terrain Contact With an Active Tail," IEEE/RSJ International Conference on Intelligent Robots and Systems, Madrid, Spain, Oct. 1–5, pp. 2739–2746.
- [17] Libby, T., Johnson, A. M., Chang-Siu, E., Full, R. J., and Koditschek, D. E., 2016, "Comparative Design, Scaling, and Control of Appendages for Inertial Reorientation," IEEE Trans. Rob., 32(6), pp. 1380–1398.
- [18] Machairas, K., and Papadopoulos, E., 2015, "On Quadruped Attitude Dynamics and Control Using Reaction Wheels and Tails," European Control Conference, Linz, Austria, July 15–17, pp. 753–758.
- [19] Mallison, H., 2010, "CAD Assessment of the Posture and Range of Motion of Kentrosaurus Aethiopicus HENNIG 1915," Swiss J. Geosci., 103(2), pp. 211–233.
- [20] Rone, W., and Ben-Tzvi, P., 2016, "Dynamic Modeling and Simulation of a Yaw-Angle Quadruped Maneuvering With a Planar Robotic Tail," J. Dyn. Syst. Trans. ASME, 138(8), p. 084502.
- [21] Santiago, J. L. C., Godage, I. S., Gonthina, P., and Walker, I. D., 2016, "Soft Robots and Kangaroo Tails: Modulating Compliance in Continuum Structures Through Mechanical Layer Jamming," Soft Rob., 3(2), pp. 54–63.
- [22] Saab, W., Rone, W., and Ben-Tzvi, P., 2018, "Discrete Modular Serpentine Robotic Tail: Design, Analysis and Experimentation," Robotica, 36(7), pp. 994–1018.

- [23] Simon, B., Sato, R., Choley, J. Y., and Ming, A., 2018, "Development of a Bio-Inspired Flexible Tail Systemss," 12th France-Japan and 10th Europe-Asia Congress on Mechatronics, Tsu, Japan, Sept. 10–12, pp. 230–235.
- [24] Rone, W. S., Saab, W., and Ben-Tzvi, P., 2018, "Design, Modeling, and Integration of a Flexible Universal Spatial Robotic Tail," ASME J. Mech. Rob., 10(4), p. 041001.
- [25] Saab, W., Rone, W. S., Kumar, A., and Ben-Tzvi, P., 2019, "Design and Integration of a Novel Spatial Articulated Robotic Tail," IEEE/ASME Trans. Mechatron., 24(2), pp. 434–446.
- [26] Liu, Y., Wang, J., and Ben-Tzvi, P., 2019, "A Cable Length Invariant Robotic Tail Using a Circular Shape Universal Joint Mechanism," ASME J. Mech. Rob., 11(5), p. 051005.
- [27] Rone, W. S., Liu, Y., and Ben-Tzvi, P., 2019, "Maneuvering and Stabilization Control of a Bipedal Robot With a Universal-Spatial Robotic Tail," Bioinspiration Biomimetics, 14(1), p. 016014.
- [28] Saab, W., Yang, J., and Ben-Tzvi, P., 2018, "Modeling and Control of an Articulated Tail for Maneuvering a Reduced Degree of Freedom Legged Robot," IEEE/RSJ International Conference on Intelligent Robots and Systems, Madrid, Spain, Oct. 1–5, pp. 2695–2700.
- [29] Trivedi, D., Rahn, C. D., Kier, W. M., and Walker, I. D., 2008, "Soft Robotics: Biological Inspiration, State of the Art, and Future Research," Appl. Bionics Biomech., 5(3), pp. 99–117.
- [30] Tanev, T. K., 2000, "Kinematics of a Hybrid (Parallel–Serial) Robot Manipulator," Mech. Mach. Theory, 35(9), pp. 1183–1196.
- [31] Merlet, J. P., 2006, Parallel Robots, Springer, Berlin.
- [32] Fan, C., Liu, H., and Zhang, Y., 2013, "Type Synthesis of 2T2R, 1T2R and 2R Parallel Mechanisms," Mech. Mach. Theory, 61, pp. 184–190.
- [33] Hess-Coelho, T. A., 2006, "Topological Synthesis of a Parallel Wrist Mechanism," ASME J. Mech. Des., 128(1), pp. 230–235.
- [34] Gosselin, C. M., and Caron, F., 1999, "Two Degree-of-Freedom Spherical Orienting Device," U.S. Patent 5,966,991.
- [35] Zeng, D., and Huang, Z., 2011, "Type Synthesis of the Rotational Decoupled Parallel Mechanism Based on Screw Theory," Sci. China Technol. Sci., 54(4), pp. 998–1004.
- [36] Kong, X., 2010, "Forward Displacement Analysis of a 2-DOF RR-RRR-RRR Spherical Parallel Manipulator," IEEE/ASME International Conference on Mechatronic and Embedded Systems and Applications, Qingdao, China, July 15–17, pp. 446–451.
- [37] Cammarata, A., 2015, "Optimized Design of a Large-Workspace 2-DOF Parallel Robot for Solar Tracking Systems," Mech. Mach. Theory, 83, pp. 175–186.
- [38] Gao, F., Li, W., Zhao, X., Jin, Z., and Zhao, H., 2002, "New Kinematic Structures for 2-, 3-, 4-, and 5-DOF Parallel Manipulator Designs," Mech. Mach. Theory, 37(11), pp. 1395–1411.
- [39] Kuo, C. H., and Dai, J. S., 2013, "Task-oriented Structure Synthesis of a Class of Parallel Manipulators Using Motion Constraint Generator," Mech. Mach. Theory, 70, pp. 394–406.
- [40] Carricato, M., and Parenti-Castelli, V., 2004, "A Novel Fully Decoupled Two-Degrees-of-Freedom Parallel Wrist," Int. J. Rob. Res., 23(6), pp. 661–667.
- [41] Heo, P., Gu, G. M., Lee, S. J., Rhee, K., and Kim, J., 2012, "Current Hand Exoskeleton Technologies for Rehabilitation and Assistive Engineering," Int. J. Precis. Eng. Manuf., 13(5), pp. 807–824.
- [42] Gogu, G., 2005, "Mobility of Mechanisms: a Critical Review," Mech. Mach. Theory, 40(9), pp. 1068–1097.
- [43] Featherstone, R., 2014, Rigid Body Dynamics Algorithms, Springer, Berlin.